Cement and Concrete Composites 140 (2023) 105104

Contents lists available at ScienceDirect

Cement and Concrete Composites

journal homepage: www.elsevier.com/locate/cemconcomp

Assessment of pore structure characteristics and tortuosity of 3D printed concrete using mercury intrusion porosimetry and X-ray tomography

Manu K. Mohan [a], A.V. Rahul [b], Jeroen F. Van Stappen [c], Veerle Cnudde [c,d], Geert De Schutter [a], Kim Van Tittelboom [a,*]

[a] Magnel-Vandepitte Laboratory, Department of Structural Engineering and Building Materials, Ghent University, Belgium
[b] Department of Civil and Environmental Engineering, Indian Institute of Technology Tirupati, India
[c] PProGRess–UGCT, Department of Geology, Faculty of Science, Ghent University, Belgium
[d] Environmental Hydrogeology, Department of Earth Sciences, Utrecht University, the Netherlands

ARTICLE INFO

Keywords:
Concrete 3D printing
Porosity
Mercury intrusion porosimetry
X-ray micro-tomography
Tortuosity
Surface fractal dimension

ABSTRACT

Extrusion-based concrete 3D printing is being increasingly used in the construction industry. This paper gives insights into the porosity and pore structure of 3D printed concrete elements using mercury intrusion porosimetry, and X-ray micro-computed tomography. The experiments were conducted with two different cement systems; among which a Portland cement-blast furnace slag blend and a calcium sulfoaluminate cement-limestone blended system. The study reveals that the interlayer region contains larger and interconnected pores with low tortuosity, which could lead to enhanced transport of ions. Using the MIP data, surface fractal dimension and tortuosity parameters were computed. It was observed that the calcium sulfo aluminate-limestone blended system has higher pore complexity and tortuosity than the Portland cement-blast furnace slag system. Compared to mercury intrusion porosimetry, the X-ray micro-computed tomography technique was able to characterize both open and closed pores present in the printed sample at the resolution of the scanning. A significantly higher open porosity and the presence of more elongated pores with a high aspect ratio were observed in the interlayer compared to the bulk region. The current study can be useful in understanding the transport of ions through different regions in printed elements to assess its durability performance.

1. Introduction

Extrusion-based 3D concrete printing (3DCP) is an emerging field and has the potential to change the construction industry [1–3]. In a typical 3DCP process, a concrete element is constructed with a computer model and by layer-wise deposition. The fresh cementitious material is usually pumped to the print head using a progressive-cavity pump and then deposited through the nozzle of concrete 3D printer to achieve the desired shape. This technique allows for greater geometrical freedom, possibilities of topological optimization & hybridization and enhanced sustainability [1,4–7].

Although 3DCP is getting wider attention, as in the case of any novel technology, there are many challenges to overcome for its use in large-scale construction projects. One such challenge is the lack of fusion between the layers, which could result in lower mechanical and durability performances [8]. The main reason for this lack of layer fusion is the surface moisture loss from the deposited layers, which, in turn, depends on environmental factors such as ambient temperature, relative humidity and wind speed [9,10]. Keita et al. [11] reported that the interlayer bond strength could reduce by 50% if the time gap between two successive layers becomes more than 1 h. On the other hand, studies have shown that if the deposited layer is protected from evaporation, the interlayer bond strength does not reduce with increasing interlayer time gap [11]. Other reported mechanisms for lack of fusion include air entrapment, which occurs mainly due to two reasons; either the deposited layers have significant surface roughness or air is entrapped during the pumping and extrusion process [12,13]. Le et al. [14] reported that the printed concrete elements may have a higher volume and size of air voids in comparison to mould cast concrete elements. In addition to that, thixotropic behaviour of the printable mixtures, formation of the lubricating layer during pumping, print parameters (such as nozzle stand-off distance and print velocity), could affect the porosity and interlayer bond strength of 3D printed concrete elements [8,10,11,15]. Another important mechanisms behind the lack of fusion is the

* Corresponding author.
E-mail address: kim.vantittelboom@ugent.be (K. Van Tittelboom).

https://doi.org/10.1016/j.cemconcomp.2023.105104
Received 20 January 2022; Received in revised form 7 February 2023; Accepted 24 April 2023
Available online 5 May 2023

moisture transport between the freshly deposited layer and to the more drier previous layer [10,16].

Literature focusing on the implications of lack of fusion in 3D printed concrete elements are scarce. The lack of layer fusion in 3DCP could result in a distinct durability performance in comparison to conventional mould cast concrete [1]. This has, for instance, been studied through neutron radiography of water uptake in printed samples and noticed that for longer interlayer time gaps, a much higher water uptake through the layer interfaces occurred was observed as compared to the bulk region of the 3D printed concrete elements [16,17]. Previous studies on conventional concrete have shown that the transport of ions through porous media like concrete is dependent on the tortuous nature of the pores present in the system [18–20]. Dhandapani and Santhanam [20] reported that the chloride penetrability of the cement paste is reduced with the increasing tortuosity of the pore network. Also, it has been indicated in literature that by making use of tortuosity and chloride binding coefficient, the service life of the concrete structures can be simulated [21]. However, in-depth studies focusing on the pore structure characteristics such as pore connectivity and tortuosity for 3D printed concrete elements are not been investigated before. Therefore, assessing these parameters of 3D printed concrete elements and a quantitative comparison with corresponding mould cast concrete samples could give insights into the transport of ions through the element and, thus, the durability performance of 3D printed concrete.

In a recent study, Van den Heever et al. [22] outline different experimental techniques available in literature for the assessment of porosity and pore structure characteristics of 3D printed concrete. One of most popular porosity characterization techniques is mercury intrusion porosimetry (MIP) [10]. It is one of the most versatile methods which can characterize a wide range of pore sizes. However, due to the injection of pressurized mercury into the sample, the possibility of destruction of the microstructure and thereby erroneous results is a possibility. Therefore, extreme care must be taken during MIP measurements. Another disadvantage of MIP tests is erroneous results can happen due to the presence of ink-bottle pores in the sample [23,24]. Several studies characterized the porosity of concrete using X-ray microtomography (X-ray μCT) [9,10,22,25–27]. In X-ray μCT, a 3D volume of X-ray images will be segmented to calculate porosity and obtain 3D quantitative information of the pore network. One of the advantages of this technique is that it is non-destructive and therefore does not cause damage to the sample. This allows monitoring pore changes in the function of time [28]. Based on the X-ray μCT closed pores, defined as empty spaces fully surrounded by material on all sides, and open pores, defined as empty spaces not fully enclosed, but at some point in 3D it is connected to the space outside of the object, can be distinguished and quantified. The pore size range that can be detected depends on the selected voxel size and field of view, limited by the sample size and equipment characteristics. One of the challenges when using X-ray μCT is that there is a trade-off between sample size and resolution. When working with concrete of 1 cm diameter, typically pore sizes in the range of 10–20 μm are possible to detect. Another reported a method to study porosity is air void analysis, which is an agile and simple method [10,27]. As a single method that captures all the pore features does not exist, a combination of MIP and X-ray μCT tests was used in the present study.

There are different ways to determine the tortuosity of a porous system. Using the formation factor approach, the tortuosity (known as electrical tortuosity) can be computed, which is indicative of the traverse path of charged ionic species (i.e., the diffusive pathway of an ion) in the porous system [20,29]. Using the pore structure characteristics, one could determine the tortuosity from the mercury intrusion porosimetry (MIP) data [30]. Another important parameter that could influence the transport of ions through the pore network and thus the durability, is the pore wall complexity. Studies have shown that the rate and extent of transport depend on how complex is the pore structure. However, the pore structure of cement-based materials and especially for 3D printed elements is extremely complicated and irregular, which is difficult to be described in terms of geometrical features. The surface fractal dimension approach is widely applied to investigate the pore structure of cement-based materials [31–34]. Using the fractal dimension values, one could get an indication of the pore complexity. Typically, the higher the surface fractal dimension, the more complex pore walls will become. The fractal dimension of porous materials could be assessed using different experimental techniques such as MIP, small-angle scattering of X-rays/neutrons, nuclear magnetic resonance, scanning electronic microscopy, nitrogen adsorption/desorption etc. [35–39]. Therefore, together with the tortuosity and pore wall complexity assessment, insights into the transport behaviour of the 3D printed concrete elements can be obtained.

Though there exist a handful of studies focusing on the pore structure of 3D printed concrete elements [1–6], all of them look into the problem from a process point of view. For instance, almost all the studies discuss the effect of the interlayer time gap, nozzle dimensions, nozzle stand-off distance, etc. On the pore structure of the resulting 3D printed elements. However, there are no studies examining the effect mixture related parameters on the pore structure characteristics. 3D printbale mixtures are significantly deifferent from the traditional mould-cast concrete due to the higher binder content and lack of coarse aggregates [40–42]. The present study focuses on the implications of using two different binder types with significantly different hydration characteristics (such as PC-based, and CSA-based) on pore structure. The effect of binder type is also very important as it can have significantly different hydration characteristics, phase assemblage and pore refinement characteristics. Due to the difference in the phase assemblage of hydration products, it is found that a significantly different pore structure can occur both in the bulk and interlayer region of 3DCP elements made with different binder types. Also, tortuosity and complexity of the pore structure can be critical factors that influence ionic transport in cementitious systems. The present study attempts to give further insights into the porosity and pore structure characteristics such as pore connectivity, tortuosity and pore complexity of the 3D printed concrete elements. For this, a combination of two different pore characterization techniques is used, MIP for characterising the open porosity and pore connectivity characteristics and X-ray μCT for characterizing both the open and closed pores as well as to obtain a 3D visualization of the pore network. An important note is that all pores, that are considered to be “closed” might be in contact with the outer area of the sample if the connections are below the resolution, and therefore, invisible. Studies are performed on samples printed at two different interlayer time gaps and using two different binder systems having different hydration characteristics. The current study could provide insights into the transport properties of the 3D printed concrete elements and thus the long-term durability behaviour.

2. Methodology

2.1. Materials and mixtures

Portland cement (PC) conforming to EN 197–1 [43], ground granulated blast furnace slag (GGBS) conforming to EN 15167–2 [44], and calcium sulfoaluminate (CSA) cement were the binders used in this study. Limestone powder was used to partially replace the CSA cement. The chemical composition and physical characteristics of these materials are listed in Table 1. A polycarboxylic ether-based superplasticizer, cellulose ether-based viscosity modifying agent and di-sodium tetraborate decahydrate (also known as borax) were used as the chemical admixtures. Fine aggregates with a maximum particle size of 2 mm were used in the formulation. The particle size distribution (PSD) of the used PC, GGBS, CSA, and limestone powder were determined by Malvern laser particle sizer. PSD of the fine aggregate was determined by sieve analysis. PSD of all the powder materials are shown in Fig. 1. Potable water was used to make the concrete mixtures. About 50 L mixture was prepared in a pan mixer for the experiments with the following

Table 1
Chemical composition and physical properties of the binders.

Oxide	Quantity (% by mass)			
	PC	GGBS	CSA	Limestone
CaO	64.30	37.97	41.5	56.6
SiO_2	18.30	35.60	8.14	0.4
Al_2O_3	5.20	13.12	23.20	0.2
Fe_2O_3	4.00	0.37	1.05	0.1
$(Na_2O)_e$	0.32	0.74	0.86	0.0
MgO	1.40	7.24	3.22	0.4
SO_3	3.50	7.24	18.36	0.1
LOI	1.40	0.95	1.45	42.2
Blaine area (m^2/kg)	408	428	500	428
Specific gravity	3.15	2.8	3.15	2.71

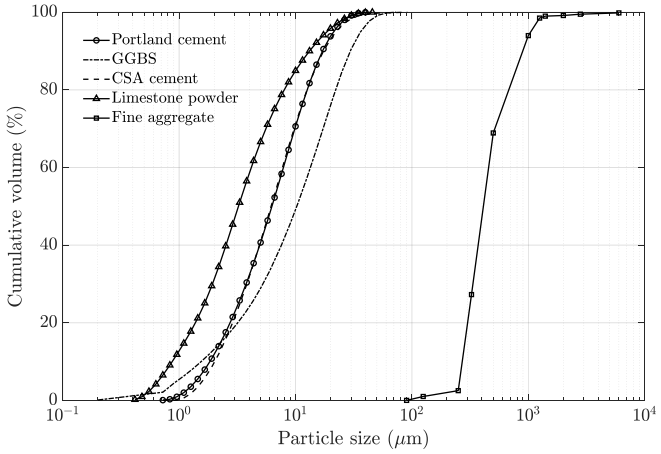

Fig. 1. Particle size distribution curve of the binders, limestone powder and fine aggregate.

procedure. (1) dry mixing of binders and fine aggregates for 60 s, (2) adding water + superplasticizer for the PC-GGBS mixture and borax dissolved water + superplasticizer for the CSA-LS mixture to the dry mixture and continue mixing for 3 min. After the mixing process, the fresh mixture was transported to the pump and used for 3D printing experiments. Also, part of the fresh mixture was filled in moulds, vibrated and covered with plastic sheets to avoid evaporation.

Two different 3D printable mixtures were used in this study. The compositions of these mixtures are listed in Table 2. These mixtures were developed as part of a bigger project (3D2BGreen project [45]) to improve the sustainability of 3D printable mixtures. Also, it must be noted that the hydration characteristics and pore refinement of these two binder systems are distinct from each other which makes them interesting and brings out novel results. The details of the mixture design process are available in the previous publications of the authors [46,47].

Table 2
Composition of the 3D printable mixtures.

Material	Quantity (kg/m^3)	
	PC-GGBS	CSA-LS
PC	376.3	–
GGBS	376.3	–
CSA cement	–	560.5
Limestone powder	–	240.2
Fine aggregate	1279.3	1201.0
Water	263.4	280.2
Borax	–	4.84
Superplasticizer	5.3	2.9
Viscosity modifying agent	0.80	0.81
Fine aggregate/binder	1.7	1.5

2.2. 3D printing and sample preparation

3D printing experiments were carried out using a six-axis industrial robot (ABB IRB6650) with a payload capacity of 125 kg and operational range of 3.2 m. The six degrees of freedom of the industrial robot enable to print in almost every orientation and tool alignment [48–50]. The industrial robot is connected with a progressive cavity pump with a discharge rate ranging between 0 and 29 L/min. The pump has motor power of 3 kW and can pump the materials at a maximum pressure of 40 bars. Two series of two-layered wall elements (length = 1000 mm, width = 40 mm, and layer thickness = 10 mm) with a were printed in two different series. (i) first series for which deposition of the second layer occurred immediately after the first layer and (ii) second series for which a time gap of 10 min after the first layer. For future reference, printed element with 0 and 10 min interlayer time gap are denoted as PC-GGBS-0 and PC-GGBS-10, respectively, for the PC-GGBS mixture, while for the CSA-LS mixture, they are denoted as CSA-LS-0 and CSA-LS-10, respectively. Also, the corresponding mould cast concrete elements were prepared with 40 × 40 × 160 mm moulds. The mould cast elements were denoted as PC-GGBS-MC and CSA-LS-MC, respectively. Figs. 2 and 3 show a 3D printed two-layered wall element and the locations at which the specimens for MIP and X-ray μCT experiments were extracted, respectively. Similar way, the samples for MIP and X-ray μCT tests were extracted from the mould cast samples also. and One day after printing, the printed samples were transferred to a curing room to be maintained at 95% relative humidity and 20 °C temperature. The samples were stored in the curing room for up to 7 days, and after which the specimens for MIP and X-ray μCT were extracted from the cured specimens. For the MIP experiments, 10 × 10 × 20 mm^3 samples were cut out from the wall elements using a diamond saw cutter. For X-ray μCT tests, 16 mm diameter and 20 mm long cylindrical cores were drilled out in the longitudinal direction with an interlayer in the middle. After that, the specimens were immersed in isopropyl alcohol for 4 days to stop the hydration following the procedures mentioned in Refs. [51, 52]. Also, the volume ratio of isopropyl alcohol and specimens were kept at about 12 for each specimen immersion. After 4 days of immersion in isopropyl alcohol, specimens were transferred to a vacuum desiccator at least for 3 days before starting the MIP and X-ray μCT experiments.

2.3. Mercury intrusion porosimetry

MIP experiments were carried out using a Pascal 140–440 porosimeter machine by Thermo scientific. The experiments were conducted at a mercury pressure ranging from vacuum pressure to 200 MPa, even though the machine was capable of exerting a maximum pressure of 400 MPa. This was to avoid the possibility of crack formation and destruction of the pore structure of the specimens due to high-pressure mercury intrusion [53]. The surface tension and contact angle of mercury were taken as 482 mN/m and 142°, respectively. Before the MIP test on the specimen, a blank run for differential mercury compression was carried out, and appropriate corrections for the mercury volume compression

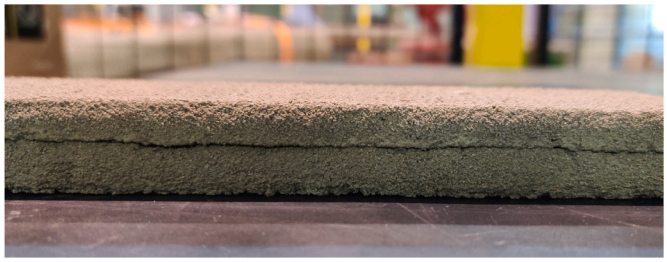

Fig. 2. 3D printed two-layered wall element.

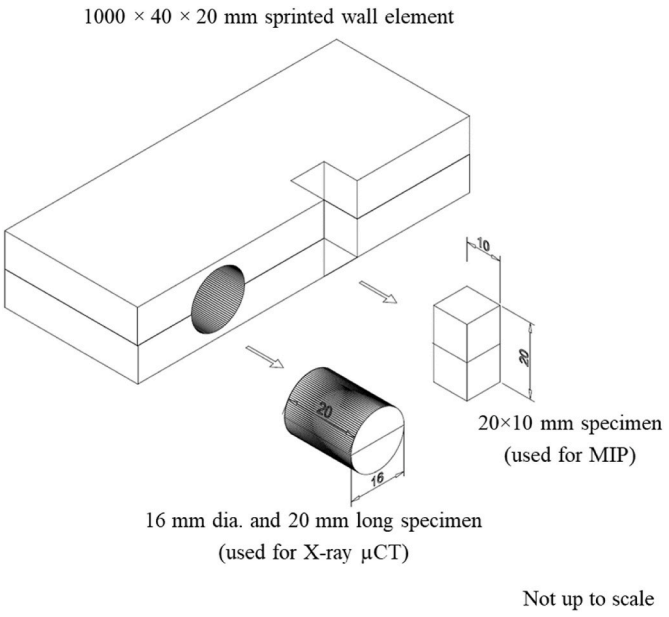

Fig. 3. Locations of the specimens extracted from the two-layer wall elements for MIP and X-ray μCT tests.

were applied [54]. The pore sizes corresponding to each pressure increment of the specimens were computed using the Washburn equation by assuming the pores had a cylindrical shape [55]. Experiments were carried out twice to check the repeatability of the results. However, in the total porosity and critical pore entry diameter curves, only one representative curve is shown.

2.4. X-ray micro-computed tomography

X-ray μ-CT studies can be used to obtain a 3D visualization of the pore structure in cement-based materials [56,57]. In the current study, tomography analysis was performed using HECTOR [58], a custom-made system developed by the Ghent University Centre for X-ray tomography (UGCT). The machine has an X-ray source of up to 240 kV and a flat-panel detector (PerkinElmer 1620 CN3 CS). As indicated earlier in section 2.2, the experiments were performed using cylindrical samples extracted from two-layered printed elements (see Fig. 3). The resolution of the scan was 18 μm. The 3D reconstruction of the raw projections was performed using the Octopus Reconstruction software [59]. Detailed image analysis on the reconstructed volume was then performed using the Octopus Analysis software [60] to determine the open and closed porosity both at the interlayer and bulk region. In addition, the aspect ratio of the pores present in both the bulk and interlayer region were also characterized. This will be later explained in section 3.2.

3. Results and discussions

3.1. Mercury intrusion porosimetry

3.1.1. Total porosity and critical pore diameter

Fig. 4 (a) and (b) show the cumulative pore volume of the PC-GGBS and CSA-LS mixtures printed at two different time intervals and the corresponding mould cast concrete mixture. The porosity values calculated from the cumulative pore volume curves are given in column 2 of Table 3. Mould cast samples have almost 20% lower total porosity compared to the 3D printed samples for PC-GGBS systems. At the same time, for the CSA-limestone mixture, the mould cast samples have almost 50% lower total porosity compared to 3D printed samples. A similar trend can also be observed in the case of tortuosity values as well.

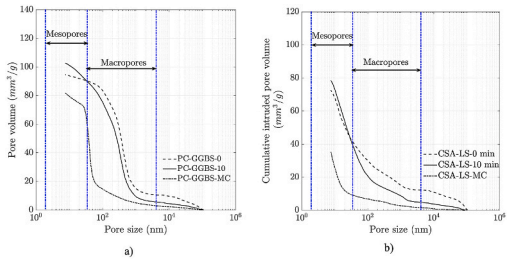

Fig. 4. Cumulative intruded pore volume vs. pore size of the mould cast and printed samples prepared with the (a) PC-GGBS mixture and the (b) CSA-LS mixture.

Table 3
Total porosity, critical pore diameter and mean distribution radius of the different mixtures obtained from MIP study.

Sample	Total porosity (%)	Critical pore diameter (nm)	Mean distribution radius (nm)
PC-GGBS-0	21.8	412.8	274.4
PC-GGBS-10	23.6	356.1	256.0
PC-GGBS-MC	18.8	41.1	41.3
CSA-LS-0	16.6	14.1	53.0
CSA-LS-10	17.9	20.2	35.1
CSA-LS-MC	8.0	8.3	13.5

This can be due to the difference in hydration and pore refinement characteristics of the two different mixtures considered in the study. As Fig. 4 contains the pore volumes corresponding to a range of pore sizes from air voids to micro-cracks, it is interesting to get more information on the different categories of pores and the corresponding volume of the pores in each category. According to the International Union of Pure and Applied Chemistry system, the pore sizes can be classified into four different categories among which (i) micropores with a pore radius less than 1.25 nm, (ii) mesopores with a radius between 1.25 and 25 nm (iii) macropores with a radius between 25 and 5000 nm and (iv) entrained and entrapped air voids and microcracks with pore radius larger than 5000 nm. The vertical lines in Fig. 4 indicate the transition from each category in the system, and the pore volumes corresponding to each pore size category are shown in Fig. 5. It can be seen that the porosity values in the macropore range are higher than the mesopore region for the 3D printed samples compared to the mould cast samples in the case of PC-GGBS mixture. On the other hand, for the CSA-LS mixtures, the porosity values in the mesopore range is higher than that in the macropore region for both the 3D printed and mould cast samples. In general, mesopores and macropores constitute the capillary porosity, whereas the micropores constitute part of the calcium silicate hydrate gel [61]. Therefore, it can be concluded that the total volume of capillary pores increases in the 3D printed compared to the mould cast concrete. Previous studies on 3D printed concrete showed similar results [10,62,63]. This can be attributed to the presence of interconnected pores at the interlayer region. Another plausible explanation is the easier moisture loss from printed samples than from mould-cast samples. This can result in a lower amount of water available for cement hydration generating more capillary pores [63,64].

Fig. 6 shows the differential intrusion curves of the different mixtures. The critical pore diameter corresponds to the peak in the differential intrusion pore curve and indicates the pore size corresponding to the maximum volume intrusion that occurs at this diameter. The critical pore diameter values are given in column 3 of Table 3. It can be seen that the critical pore sizes of the CSA cement-based mixtures are significantly lower than those of the PC-GGBS mixtures for both the printed and mould cast samples. Similar to the trend observed in total porosity, for

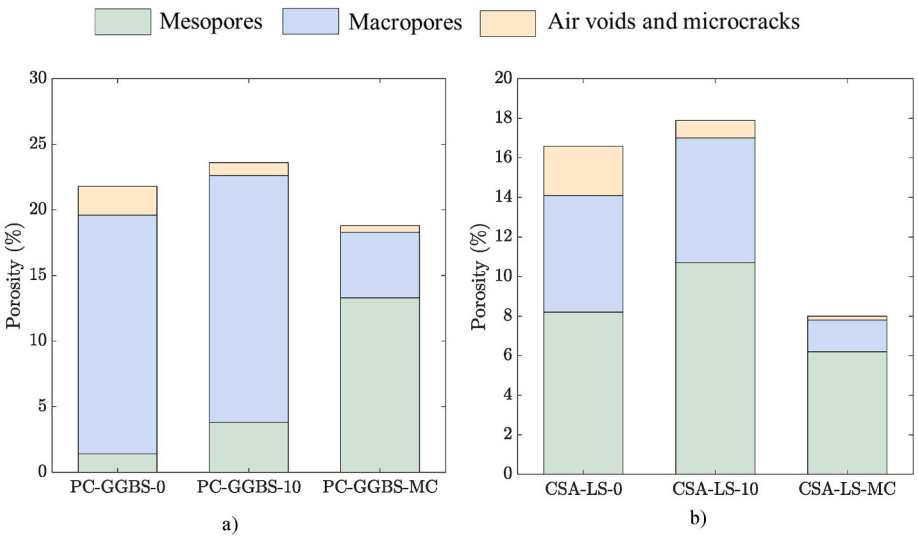

Fig. 5. Porosity values corresponding to each pore size category for the (a) PC-GGBS and (b) CSA-LS mixtures.

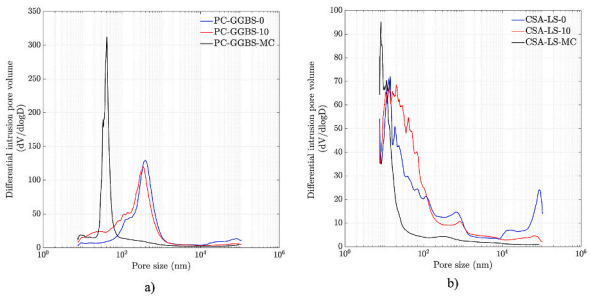

Fig. 6. Differential intrusion pore volume vs pore sizes of the mould cast and printed samples (a) PC-GGBS mixture, (b) CSA-LS mixture.

both the mixtures, the critical pore diameter is higher for 3D printed compared to the mould cast samples. Higher critical pore diameters were also reported previously [63]. Also, it can be noticed that with the increase in the time gap of layers, the critical pore diameter slightly decreases for PC-GGBS mixtures and at the same time, the critical pore entry diameter slightly increases for the CSA-limestone mixtures.

3.1.2. Pore connectivity and tortuosity

As outlined in the introduction section, attempts were made previously to correlate the transport parameters with the tortuosity of the system [20,65–67]. Tortuosity is defined as the ratio of the continuous path length between two points and the shortest straight-line length [68]. The tortuosity of a porous system can be computed using the corrugated pore structure model (CPSM) [69]. According to CPS model, the tortuosity is calculated as follows:

$$\tau = 4.6242\, ln\left(\frac{4.996}{1-\alpha_{en}} - 1\right) - 5.8032 \quad (1)$$

where τ and α_{en} are the tortuosity and pore entrapment fraction, respectively. The pore entrapment fraction (α_{en}) can be defined as the ratio between the pore entrapment volume and the total intrusion volume. The pore entrapment volume can be calculated from the difference between intrusion and extrusion curves for the same applied pressure [30]. It is worth noting that the CPS model described in Eq. (1) was originally established from nitrogen desorption measurements by Salmas et al. [69]. Later the authors validated the suitability of the CPSM model with MIP and tomography experiments [70,71]. Also, the tortuosity of cement-based materials was successfully computed for cement-based materials using the CPSM model applied on MIP data [30,72].

Fig. 7 shows the tortuosity values calculated using Eq. (1) for the different printed and mould cast samples. It can be seen that the tortuosity of the PC-GGBS mixtures is lower than that of the CSA-LS mixtures for both the printed and mould cast samples. The higher tortuosity in the case of the CSA cement-based mixtures could be attributed to the enhanced pore refinement and faster rate of hydration [73]. The enhanced pore refinement occurs due to precipitation and densification of the ettringite crystals at the empty pores of the C–S–H matrix [60]. Also, the tortuosity of the printed samples is much lower than that for the corresponding mould cast concrete samples for both the PC-GGBS and CSA-LS mixture. The lower tortuosity indicates the more connected pathways for the transport of moisture and ions [68]. In case of the 3D printed elements, due to the presence of interlayer regions with more interconnected pores, the tortuosity becomes lower. A very slight increase in the tortuosity can be observed for the CSA-limestone systems considering the error bars. However, the changes in tortuosity are negligible for the PC-GGBS mixture with an increase in the interlayer time gap. This could be due to the relatively short interlayer time gap

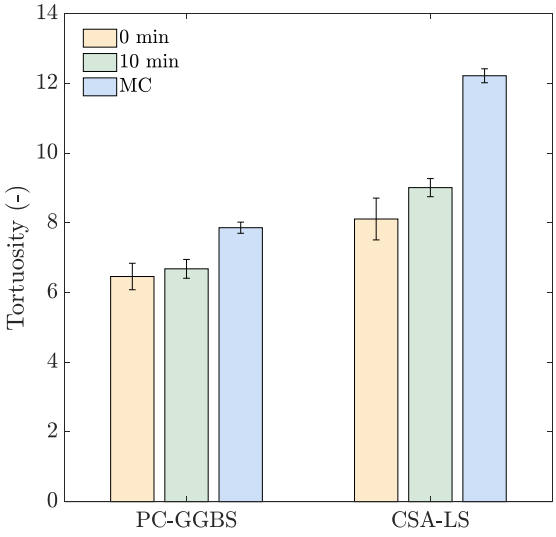

Fig. 7. Tortuosity values of the 3D printable mixtures with different time gaps of deposition between the two layers and comparison with mould cast mixture (error bar indicates the standard deviation from the mean value).

(10 min) used in the current study. In a recent study, Dressler et al. [74] characterised the tortuosity of shotcrete 3D printed concrete samples with different dosages of accelerator and having interlayer time gaps of 0–30 min using X-ray computed tomography. Also, in their study, for mixtures without accelerator, no significant variation in tortuosity was observed with an increase in the interlayer time gap [74].

3.1.3. Pore complexity from MIP

As mentioned in the introduction section, the transport of ions depends on the geometric features of the pores present in the system. The geometric complexity of the pores can be understood from the surface fractal dimension (D). Literature indicates that the fractal dimensions of pores can be correlated with conductivity (both thermal and electrical), permeability, diffusivity and mechanical strength, as these properties are intimately related to the pore structure. In general, the topological fractal dimension of a surface surrounding a volume lies between 2 and 3 depending on the complexity or roughness of the surface [75]. Typically, MIP results are computed by considering cylindrical-shaped pores with a fractal dimension of two; however, there is a high probability that the pore walls are rough, and it can be inferred that the volume of pores, in reality, depends on the scale at which the measurements are carried out. The scaling relationship of the fractal surface area of pore walls and the corresponding volume encompassed by the surface can be computed using the correlation put forward by Mandelbrot [76] as follows:

$$S^{1/D} \sim V^{1/3} \tag{2}$$

where S is the surface area (mm^2), and V is the volume (mm^3) encompassed by the surface. During MIP, the surface energy in the system will be equal to the work done for the mercury to intrude into the pores of the specimen. Zhang and Li [35] proposed a linear relationship between the accumulated work W_n, (J) and accumulated intrusion surface Q_n, (J) in logarithmic scale, as follows:

$$ln(W_n) = C + ln(Q_n) \tag{3}$$

where C is a constant of proportionality, and subscript n refers to a certain intrusion phase. Accumulated intrusion work and accumulated intrusion surface can be determined as follows:

$$W_n = \sum_{i=1}^{n} P_i \Delta V_i \text{ and } Q_n = {r_n}^{2-D} {V_n}^{D/3} \tag{4}$$

where V is the accumulated volume (mm^3) of mercury and r_n i s the corresponding pore radius and D is the fractal dimension. Rearranging Eqs. (3) and (4), one can get the following expression to calculate the surface fractal dimension (D) from the MIP data [77]

$$ln\left(\frac{W_n}{{r_n}^2}\right) = Dln\left(\frac{{V_n}^{1/3}}{r_n}\right) + C \tag{5}$$

The scale-dependent surface fractal dimension could give an indication of the complexity or roughness of the pore wall structure as observed in the case of cement-based systems [39,75,78,79] and other porous materials [77].

Figs. 8 and 9 show plots of the cumulative intrusion work versus the cumulative surface energy for the PC-GGBS and CSA-LS mixtures, respectively. The plot can be subdivided into three regions and in which two regions have fractal properties: (i) macro-fractal, which corresponds

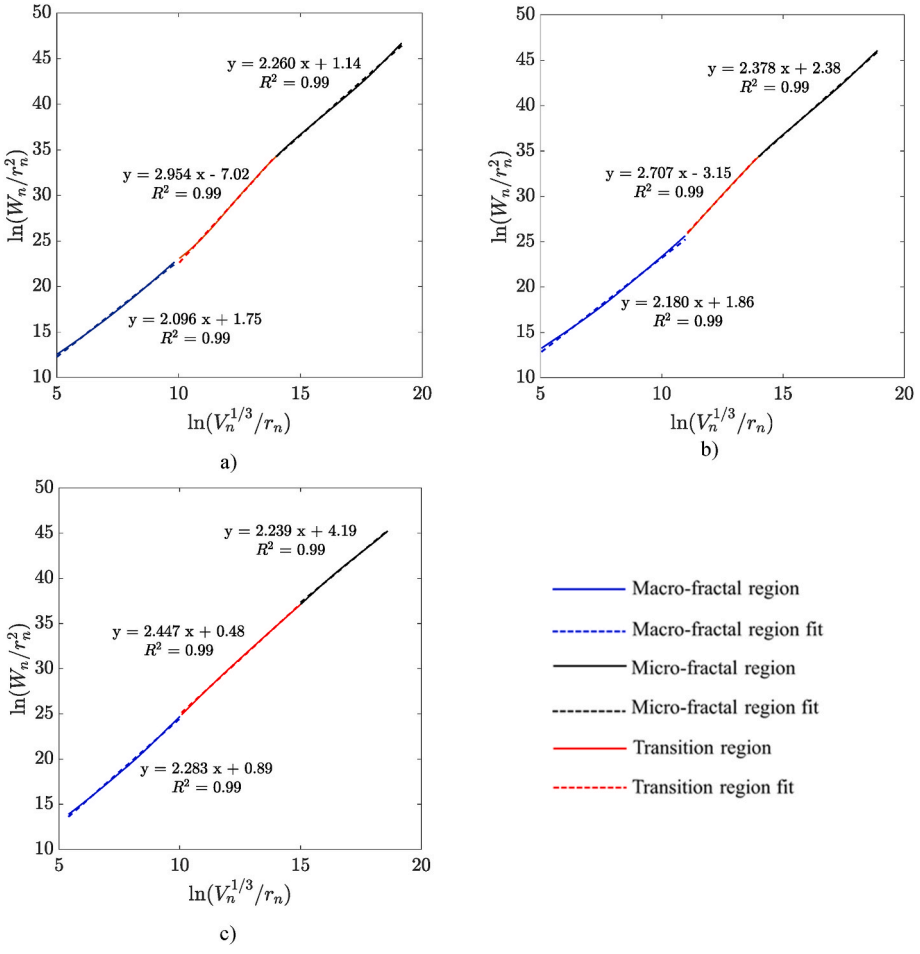

Fig. 8. Surface fractal dimension values of the PC-GGBS mixture: (a) PC-GGBS-0 (b) PC-GGBS-10 (c) PC-GGBS-MC.

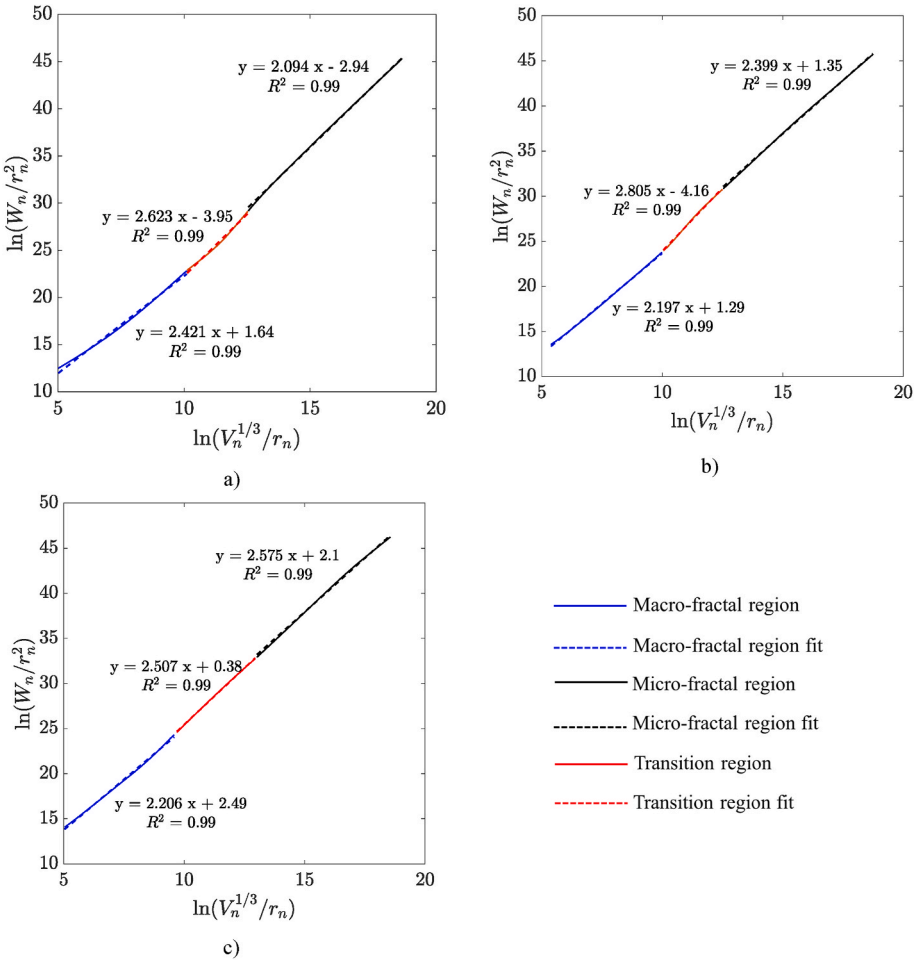

Fig. 9. Surface fractal dimension values of the CSA-LS mixture: (a) CSA-LS-0 (b) CSA-LS-10 (c) CSA-LS-MC.

to the capillary pores and, (ii) micro-fractal, which correlates to the inter-layer or inter-granular space between the hydration products present in the system. The third region is a transition region without having fractal properties. The transition region represents the smaller capillary pores within the system and does not have a clear surface fractal property [39,80]. In which two regions have fractal properties: (i) macro-fractal, which corresponds to the capillary pores and, (ii) micro-fractal, which correlates to the inter-layer or inter-granular space between the hydration products present in the system. The third region is a transition region without having fractal properties. The transition region represents the smaller capillary pores within the system and does not have a clear surface fractal property [39,80]. In Figs. 8 and 9, each of these regions is fitted with linear regression, and the slope of the fitted curve gives the fractal dimension value corresponding to each region [39].

Table 4
Surface fractal dimension values of the two mixtures being 3D printed and mould cast.

Sample name	Surface fractal dimension	
	Macro fractal	Micro fractal
PC-GGBS-0	2.096	2.260
PC-GGBS-10	2.180	2.378
PC-GGBS-MC	2.283	2.239
CSA-LS-0	2.094	2.421
CSA-LS-10	2.197	2.399
CSA-LS-MC	2.206	2.575

Table 4 shows the surface fractal dimension values of both mixtures. It can be noticed that the micro-fractal dimension values were higher for the CSA mixtures than for the PC-GGBS mixtures. On the other hand, the macro-fractal dimension values of both mixtures lie in the same range. A slight increase in the macro-fractal dimension values can be observed with the increase in the interlayer time gap. Studies have shown that there will be rapid precipitation of small and thin ettringite crystals after 24 h hydration due to the enhanced rate of hydration in the CSA cement-based systems. These ettringite crystals evolve into a very dense structure over the course of 7 days. The belite phase in CSA cement reacts slower than the ye'elimite phase and precipitates C–S–H. There could be precipitation and densification of the ettringite crystals at the empty spaces of the C–S–H matrix [81]. This could result in a more complex pore wall structure and, in turn, result in higher surface fractal dimensions. Such an extended pore refinement is not observed in the PC-GGBS system, and the surface fractal dimension values were also lower than that of the CSA-limestone system. Similar surface fractal dimension ranges were reported for the slag-blended Portland cement mixtures in the literature [75,78]. Also, it was reported that the surface fractal dimensions increase with slag substitution and hydration age and decrease with the increase in water-to-binder ratio, resulting in higher surface fractal dimensions [75,78]. Such an extended pore refinement is not observed in the PC-GGBS system, and the surface fractal dimensions were also lower than that of the CSA-limestone system. Similar surface fractal dimension ranges were reported for the slag-blended Portland cement mixtures in the literature. Also, it was reported that the surface fractal dimensions increase with slag substitution and hydration age and

decrease with the increase in water-to-binder ratio [75,78].

The influence of surface fractal dimension on the transport of ionic species has been studied before in other porous media [82,83]. Although Yu et al. [84] further extended these studies to cementitious systems and investigated the transport properties such as permeability, diffusivity and thermal conductivity using fractal-based models, more in-depth studies are needed in this regard.

3.2. Pore structure assessment from X-ray micro-computed tomography

From the tomography scans, a 3D reconstruction of the sample was first created. For instance, Fig. 10 (a) shows a slice taken from the 3D reconstruction of the CSA sample with no time gap. To quantify the pore characteristics, the background noise in the reconstructed volume was first removed using a suitable filter. Then, a region of interest (ROI) consisting of 400 × 400 × 100 voxels was selected from both the bulk and interlayer region of the printed sample, as shown in Fig. 10 (b). The ROI image matrix was then binarized using Otsu's method [85]. In the binarized image matrix shown in Fig. 10 (c), the background voxels (shown in white colour) represent the solid phases, while the foreground voxels (shown in black colour) indicate the pores. The number of foreground voxels divided by the total number of voxels present in the ROI was determined to compute the total porosity. Further using the Octopus analysis software [60], each individual pores present in the ROI was identified and labelled. This information was then used to compute the connectivity of the pore network and, thus, the open and closed porosity in the interlayer and bulk region. It must be noted that the closed pores are considered here as they do not show any connection towards the outer surface, but in reality they might be also open and connected to the outer surface by microporosity which is smaller than the resolution of the scanning (resolution = 18 μm) and therefore not visible on the CT scan. Also, it is worth noting that the open porosity in the octopus analysis software is defined as reaching the outer bounds of the ROI. When there are many individual pores, indicating very low open porosity, that does not mean that these are not connected with pores smaller than the resolution of the images. In addition, the size of a bounding box for each individual pore was computed. The maximum dimension divided by the lowest dimension of the bounding box gives a measure of the aspect ratio of the pore. An aspect ratio close to 1 represents a pore with equal size in x, y and z-direction, while a value higher than 1 indicates an elongated pore [86].

The total, open and closed porosity and the average aspect ratio of the pores present in the interlayer and the bulk region of the different samples are summarized in Table 5 Irrespective of the interlayer time gap, it can be seen that the total porosity (calculated based on the resolution of the scanning) is in the range of 12–14% for the interlayer

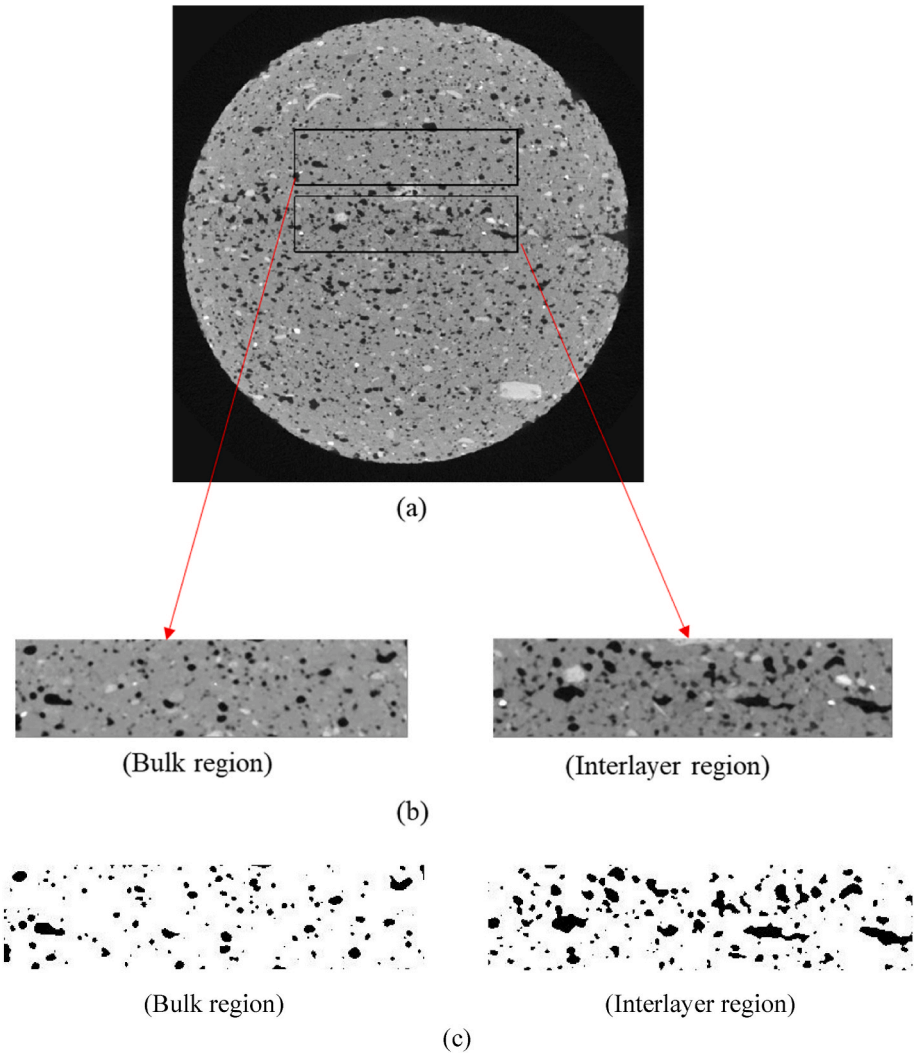

Fig. 10. (a) A slice taken from the tomographic 3D reconstruction of CSA-LS-0 sample (b) ROI (consisting of 400 × 400 × 100 voxels) from both the interlayer and bulk region and (c) The ROI after binarization (black colour indicating the pores). (For interpretation of the references to colour in this figure legend, the reader is referred to the Web version of this article.)

Table 5
Summary of results from X-ray μCT analysis.

Sample name	Region	Porosity (%)			Aspect ratio
		Open	Closed	Total	
PC-GGBS-0	Bulk	3.8	4.9	8.7	1.7
	Interlayer	8.6	4.5	13.1	3.0
PC-GGBS-10	Bulk	1.1	5.0	6.1	1.1
	Interlayer	8.0	4.5	12.5	3.4
CSA-LS-0	Bulk	2.3	5.1	7.4	1.3
	Interlayer	9.3	4.0	13.3	3.2
CSA-LS-10	Bulk	2.1	6.2	8.4	1.2
	Interlayer	7.7	4.4	12.1	3.4

region, while for the bulk region, the porosity is much lower and in the range of 7–9%. Interestingly, as seen in Table 5, even though the closed porosity is similar for both interlayer and bulk regions, the open porosity increases 2 to 3 times in the interlayer compared to the bulk region. It must be noted that the total volume of capillary pores is not captured from the X-ray μCT tests as the resolution of the X-ray μCT test was much lower than the capillary pore size ranges (up to 5 μm). Nevertheless, insights into the transport properties can be obtained by parametrically studying the influence of 3D printing process parameters and mixture-related parameters. For instance, higher open porosity indicates the likelihood of relatively faster transport of ions through the interlayer region, as already reported by a few researchers [1,16]. Another aspect to be pointed out is the difference in the total porosity computed from X-ray μCT and MIP analysis. The values obtained from MIP (Table 3) are higher as compared to those computed from X-ray μCT (Table 5). Although the latter can characterize both open and closed porosity, the resolution of the pores accessible by X-ray μCT is much lower (18 μm in the current study), while MIP can access pores ranging from nanometer-scale onwards [87]. The porosity obtained from MIP equal to or larger than the resolution of the X-ray μCT was almost 40% lower than that of porosity X-ray μCT. Another aspect is that the hydration and pore refinement of both mixtures is significantly different. The pore refinement observed in CSA-limestones systems happens at pore sizes much below the resolution of the X-ray μ CT tests. Also, it must be noted that the X-ray μCT provides the total porosity value of all pores larger than the resolution of the scanning. The resolution of the X-ray μCT could be much lower than the resolution used in the current study, depeding on the size of the samples used for the anaylsis. Although with MIP, we can access much lower pore sizes (even in the nanometer scales), by applying much higher pressure values to intrude the merucry to the sample, which could create the erraneous results due to the compression of the mercury and internal fractures on the samples [88,89].

Table 5 also indicates the average aspect ratio of the pores present in the interlayer and bulk region of the different samples. For both the bulk of the CSA and slag mixture, the average aspect ratio of the pores is in the range of 1–1.6. This indicates that the pores present in the bulk region are mostly spherical pores or have a similar size in all directions. On the other hand, for all samples, irrespective of the time gap, a much higher average aspect ratio (>3) can be observed in the interlayer region. This indicates that the pores in this region are mostly elongated in shape. A similar observation of elongated pores in the interlayer region has also been recently reported by other researchers [10,25,27]. The higher total porosity and the presence of elongated pores in the interlayer region may have arisen from reduced compaction between the deposited fresh concrete layers during the printing process.

4. Conclusions and perspectives

A multi-analytical pore assessment approach combining MIP and X-ray μCT of 3D printed concrete elements with a Portland cement-slag (PC-GGBS) blend and calcium sulfoaluminate cement-limestone (CSA-LS) blend is carried out in the present study.

From the MIP study, printed samples show higher total porosity and higher mean distribution radius compared to the mould cast specimens indicating a coarser pore size distribution. The reduction in the mean distribution is more significant in the case of the slag mixture. Also, the critical pore sizes of the printed elements made using the PC- GGBS mixture is much lower, compared to CSA-based mixture In addition, the printed concrete exhibits higher critical pore sizes than the corresponding mould cast samples indicating the possibility of higher transport of ions in printed concrete systems.

Similar trends can be observed in the tortuosity values. The tortuosity is significantly lower for printed compared to mould cast samples, possibly leading to the higher transport properties in the printed samples. Also, a higher tortuosity is associated with the CSA-LS compared to the PC-GGBS system which could be attributed to the higher pore refinement and faster rate of hydration reaction in CSA-LS system.

Pore complexity was also assessed from the MIP data using the multi-fractal dimension approach. The macro-fractal dimensions are similar for 3D printed PC-GGBS and CSA-LS blended mixtures; however, these are slightly higher for mould cast samples. On the other hand, the micro-fractal dimensions are higher for CSA-LS as compared to PC-GGBS mixtures – indicating a more complex pore structure in the micro-pore region for CSA mixtures. Together with higher tortuosity and complex pore structure, the transport of ions in CSA-limestone mixtures could be significantly lower.

The X-ray μCT studies showed the presence of a significantly higher amount of open pores in the interlayer compared to the bulk region. No significant difference was observed in either open or closed porosity when the interlayer time gap was increased from 0 to 10 min – indicating that cold joints are not present at the interlayer region. An interlayer time gap of 10 min was chosen in the present study by considering the faster construction rates. However, for slower construction rates with significant delays between the deposition of two successive layers, there could be a significant increase in open and closed porosity Further, for both mixtures, pores with a significantly higher aspect ratio (indicating elongated pores) were observed in the interlayer region. The results from the current study can be used to gain more insights into the transport properties and durability performance of PC and CSA-based 3D printed elements.

Declaration of competing interest

The authors declare that they have no known competing financial interests or personal relationships that could have appeared to influence the work reported in this paper.

Data availability

Data will be made available on request.

Acknowledgements

The authors would like to acknowledge the financial support provided by SIM (Strategic Initiative Materials in Flanders) and VLAIO (Flanders agency for innovation & entrepreneurship) towards the 3D2BGreen project. The authors also acknowledge the companies, BESIX, ResourceFull and Witteveen + Bos for being the partners of the 3D2BGreen project. The authors thankfully acknowledge the research fellows and technicians at the Magnel-Vandepitte Laboratory for their help in this study. Authors also extend their sincere gratitude towards Ecocem Benelux B.V. and supplying the GGBS and Italcementi cement for providing the CSA cement used in the study.

References

[1] M.K. Mohan, A.V. Rahul, G. De Schutter, K. Van Tittelboom, Extrusion-based concrete 3D printing from a material perspective: a state-of-the-art review, Cem. Concr. Compos. 115 (2021), 103855, https://doi.org/10.1016/j.cemconcomp.2020.103855.

[2] G. De Schutter, K. Lesage, V. Mechtcherine, V.N. Nerella, G. Habert, I. Agusti-Juan, Vision of 3D printing with concrete — technical, economic and environmental potentials, Cement Concr. Res. 112 (2018) 25–36, https://doi.org/10.1016/j.cemconres.2018.06.001.

[3] R.A. Buswell, W.R. Leal de Silva, S.Z. Jones, J. Dirrenberger, 3D printing using concrete extrusion: a roadmap for research, Cement Concr. Res. 112 (2018) 37–49, https://doi.org/10.1016/j.cemconres.2018.05.006.

[4] G. Vantyghem, W. De Corte, E. Shakour, O. Amir, 3D printing of a post-tensioned concrete girder designed by topology optimization, Autom. ConStruct. 112 (2020), 103084, https://doi.org/10.1016/j.autcon.2020.103084.

[5] C. Menna, J. Mata-Falcón, F.P. Bos, G. Vantyghem, L. Ferrara, D. Asprone, T. Salet, W. Kaufmann, Opportunities and challenges for structural engineering of digitally fabricated concrete, Cement Concr. Res. 133 (2020), 106079, https://doi.org/10.1016/j.cemconres.2020.106079.

[6] N. Roussel, Rheological requirements for printable concretes, Cement Concr. Res. 112 (2018) 76–85, https://doi.org/10.1016/j.cemconres.2018.04.005.

[7] M.K. Mohan, A.V. Rahul, B. van Dam, T. Zeidan, G. De Schutter, K. Van Tittelboom, Performance criteria, environmental impact and cost assessment for 3D printable concrete mixtures, Resour. Conserv. Recycl. 181 (2022) 106255. https://doi.org/10.1016/j.resconrec.2022.106255.

[8] J. Kruger, G. van Zijl, A compendious review on lack-of-fusion in digital concrete fabrication, Addit. Manuf. 37 (2021), 101654, https://doi.org/10.1016/j.addma.2020.101654.

[9] H. Kloft, H.W. Krauss, N. Hack, E. Herrmann, S. Neudecker, P.A. Varady, D. Lowke, Influence of process parameters on the interlayer bond strength of concrete elements additive manufactured by Shotcrete 3D Printing (SC3DP), Cem, Concr. Res. 134 (2020), 106078, https://doi.org/10.1016/j.cemconres.2020.106078.

[10] J. Van Der Putten, M. Deprez, V. Cnudde, G. De Schutter, K. Van Tittelboom, Microstructural characterization of 3D printed cementitious materials, Materials 12 (2019) 1–22, https://doi.org/10.3390/ma12182993.

[11] E. Keita, H. Bessaies-Bey, W. Zuo, P. Belin, N. Roussel, Weak bond strength between successive layers in extrusion-based additive manufacturing: measurement and physical origin, Cement Concr. Res. 123 (2019), 105787, https://doi.org/10.1016/j.cemconres.2019.105787.

[12] V.N. Nerella, S. Hempel, V. Mechtcherine, Effects of layer-interface properties on mechanical performance of concrete elements produced by extrusion-based 3D-printing, Construct. Build. Mater. 205 (2019) 586–601, https://doi.org/10.1016/j.conbuildmat.2019.01.235.

[13] B. Panda, N.A.N. Mohamed, S.C. Paul, G.V.P.B. Singh, M.J. Tan, B. Šavija, The effect of material fresh properties and process parameters on buildability and interlayer adhesion of 3D printed concrete, Materials 12 (2019), https://doi.org/10.3390/ma12132149.

[14] T.T. Le, S.A. Austin, S. Lim, R.A. Buswell, R. Law, A.G.F. Gibb, T. Thorpe, Hardened properties of high-performance printing concrete, Cement Concr. Res. 42 (2012) 558–566, https://doi.org/10.1016/j.cemconres.2011.12.003.

[15] N. Roussel, F. Cussigh, Distinct-layer casting of SCC: the mechanical consequences of thixotropy, Cement Concr. Res. 38 (2008) 624–632, https://doi.org/10.1016/j.cemconres.2007.09.023.

[16] J. Van Der Putten, M. Azima, P. Van den Heede, T. Van Mullem, D. Snoeck, C. Carminati, J. Hovind, P. Trtik, G. De Schutter, K. Van Tittelboom, Neutron radiography to study the water ingress via the interlayer of 3D printed cementitious materials for continuous layering, Construct. Build. Mater. 258 (2020) 130–137, https://doi.org/10.1016/j.conbuildmat.2020.119587.

[17] C. Schröfl, V.N. Nerella, V. Mechtcherine, Capillary water intake by 3D-printed concrete visualised and quantified by neutron radiography, in: RILEM Bookseries, Springer, Netherlands, 2019, pp. 217–224, https://doi.org/10.1007/978-3-319-99519-9_20.

[18] L. Yuan-Hui, S. Gregory, Diffusion of ions in sea water and in deep-sea sediments, Geochem. Cosmochim. Acta 38 (1974) 703–714, https://doi.org/10.1016/0016-7037(74)90145-8.

[19] M. Ben Clennell, Tortuosity: a guide through the maze, Geol. Soc. Spec. Publ. 122 (1997) 299–344, https://doi.org/10.1144/GSL.SP.1997.122.01.18.

[20] Y. Dhandapani, M. Santhanam, Investigation on the microstructure-related characteristics to elucidate performance of composite cement with limestone-calcined clay combination, Cement Concr. Res. 129 (2020), 105959, https://doi.org/10.1016/j.cemconres.2019.105959.

[21] P. Yang, Y. Dhandapani, M. Santhanam, N. Neithalath, Simulation of chloride diffusion in fly ash and limestone-calcined clay cement (LC3) concretes and the influence of damage on service-life, Cement Concr. Res. 130 (2020), 106010, https://doi.org/10.1016/j.cemconres.2020.106010.

[22] M. van den Heever, A. du Plessis, J. Kruger, G. van Zijl, Evaluating the effects of porosity on the mechanical properties of extrusion-based 3D printed concrete, Cement Concr. Res. 153 (2022), 106695, https://doi.org/10.1016/J.CEMCONRES.2021.106695.

[23] S. Diamond, Mercury porosimetry. An inappropriate method for the measurement of pore size distributions in cement-based materials, Cement Concr. Res. 30 (2000) 1517–1525, https://doi.org/10.1016/S0008-8846(00)00370-7.

[24] F. Moro, H. Böhni, Ink-bottle effect in mercury intrusion porosimetry of cement-based materials, J. Colloid Interface Sci. 246 (2002) 135–149, https://doi.org/10.1006/JCIS.2001.7962.

[25] J. Kruger, A. du Plessis, G. van Zijl, An investigation into the porosity of extrusion-based 3D printed concrete, Addit. Manuf. 37 (2021), 101740, https://doi.org/10.1016/j.addma.2020.101740.

[26] H. Lee, J.H.J. Kim, J.H. Moon, W.W. Kim, E.A. Seo, Correlation between pore characteristics and tensile bond strength of additive manufactured mortar using X-ray computed tomography, Construct. Build. Mater. 226 (2019) 712–720, https://doi.org/10.1016/J.CONBUILDMAT.2019.07.161.

[27] Y. Chen, O. Çopuroğlu, C. Romero Rodriguez, F.F.d. Mendonca Filho, E. Schlangen, Characterization of air-void systems in 3D printed cementitious materials using optical image scanning and X-ray computed tomography, Mater. Char. 173 (2021), 110948, https://doi.org/10.1016/j.matchar.2021.110948.

[28] V. Cnudde, T. De Kock, M. Boone, W. De Boever, T. Bultreys, J. Van Stappen, D. Vandevoorde, J. Dewanckele, H. Derluyn, V. Cardenes, C. Cardenes, L. Van Hoorebeke, Conservation studies of cultural heritage: X-ray imaging of dynamic processes in building materials, Eur. J. Mineral 27 (2015) 269–278, https://doi.org/10.1127/EJM/2015/0027-2444.

[29] F. Rajabipour, J. Weiss, Electrical conductivity of drying cement paste, Mater. Struct. Constr. 40 (2007) 1143–1160, https://doi.org/10.1617/s11527-006-9211-z.

[30] Q. Zeng, K. Li, T. Fen-Chong, P. Dangla, Analysis of pore structure, contact angle and pore entrapment of blended cement pastes from mercury porosimetry data, Cem. Concr. Compos. 34 (2012) 1053–1060, https://doi.org/10.1016/j.cemconcomp.2012.06.005.

[31] C. Li, L. Jiang, N. Xu, S. Jiang, Pore structure and permeability of concrete with high volume of limestone powder addition, Powder Technol. 338 (2018) 416–424, https://doi.org/10.1016/J.POWTEC.2018.07.054.

[32] S. Tang, J. Huang, L. Duan, P. Yu, E. Chen, A review on fractal footprint of cement-based materials, Powder Technol. 370 (2020) 237–250, https://doi.org/10.1016/J.POWTEC.2020.05.065.

[33] Y. Gao, J.Y. Jiang, K. Wu, Fractal modeling of pore structure and ionic diffusivity for cement paste, Adv. Mater. Sci. Eng. 2016 (2016), https://doi.org/10.1155/2016/7645954.

[34] S.W. Tang, Z.J. Li, E. Chen, H.Y. Shao, Non-steady state migration of chloride ions in cement pastes at early age, RSC Adv. 4 (2014) 48582–48589, https://doi.org/10.1039/C4RA06306F.

[35] B. Zhang, S. Li, Determination of the surface fractal dimension for porous media by mercury porosimetry, Ind. Eng. Chem. Res. 34 (1995) 1383–1386, https://doi.org/10.1021/ie00043a044.

[36] Y. Wang, S. Diamond, A fractal study of the fracture surfaces of cement pastes and mortars using a stereoscopic SEM method, Cement Concr. Res. 31 (2001) 1385–1392, https://doi.org/10.1016/S0008-8846(01)00591-9.

[37] D. Pearson, A.J. Allen, A study of ultrafine porosity in hydrated cements using small angle neutron scattering, J. Mater. Sci. 20 (1985) 303–315, https://doi.org/10.1007/BF00555924.

[38] B. Sahouli, S. Blacher, F. Brouers, Fractal surface analysis by using nitrogen adsorption data: the case of the capillary condensation regime, Langmuir 12 (1996) 2872–2874, https://doi.org/10.1021/la950877p.

[39] Q. Zeng, K. Li, T. Fen-Chong, P. Dangla, Surface fractal analysis of pore structure of high-volume fly-ash cement pastes, Appl. Surf. Sci. 257 (2010) 762–768, https://doi.org/10.1016/j.apsusc.2010.07.061.

[40] M.K. Mohan, A.V. Rahul, Y. Tao, G. De Schutter, K. Van Tittelboom, Hydration re-initiation of borated CSA systems with a two-stage mixing process: An application in extrusion-based concrete 3D printing, Cem. Concr. Res. 159 (2022) 106870. https://doi.org/10.1016/j.cemconres.2022.106870.

[41] A.V. Rahul, M.K. Mohan, G. De Schutter, K. Van Tittelboom, 3D printable concrete with natural and recycled coarse aggregates: Rheological, mechanical and shrinkage behaviour, Cem. Concr. Compos. 125 (2022) 104311. https://doi.org/10.1016/j.cemconcomp.2021.104311.

[42] A.V. Rahul, M. Santhanam, Evaluating the printability of concretes containing lightweight coarse aggregates, Cem. Concr. Compos. 109 (2020) 103570. https://doi.org/10.1016/j.cemconcomp.2020.103570.

[43] EN 197-1, Composition, Specifications, and Conformity Criteria for Common Cements, 2004.

[44] IS 16714, Ground Granulated Blast Furnace Slag for Use in Cement, Mortar & Concrete- Specification, 2018.

[45] 3D2BGREEN – SIM Flanders, (n.d.). https://www.sim-flanders.be/projects/3d2bgreen/(accessed October 25, 2022).

[46] M.K. Mohan, A.V. Rahul, K. Van Tittelboom, G. De Schutter, Rheological and pumping behaviour of 3D printable cementitious materials with varying aggregate content, Cement Concr. Res. 139 (2021), https://doi.org/10.1016/j.cemconres.2020.106258.

[47] M.K. Mohan, A.V. Rahul, G. De Schutter, K. Van Tittelboom, Early age hydration, rheology and pumping characteristics of CSA cement-based 3D printable concrete, Construct. Build. Mater. 275 (2021), 122136, https://doi.org/10.1016/j.conbuildmat.2020.122136.

[48] ABB Robotics Products, Product Manual Articulated Robot, 2010.

[49] R.A. Mosbacher, Product specification: US Product safety study. https://doi.org/10.1080/09613219308727250, 1993.

[50] G. Vantyghem, W. De Corte, M. Steeman, V. Boel, Density-based topology optimization for 3D-printable building structures, Struct. Multidiscip. Optim. 60 (2019) 2391–2403, https://doi.org/10.1007/s00158-019-02330-7.

[51] R. Snellings, J. Chwast, Ö. Cizer, N. De Belie, Y. Dhandapani, P. Durdzinski, J. Elsen, J. Haufe, D. Hooton, C. Patapy, M. Santhanam, K. Scrivener, D. Snoeck, L. Steger, S. Tongbo, A. Vollpracht, F. Winnefeld, B. Lothenbach, RILEM TC-238 SCM recommendation on hydration stoppage by solvent exchange for the study of hydrate assemblages, Mater. Struct. Constr. 51 (2018) 1–4, https://doi.org/10.1617/s11527-018-1298-5.

[52] C. Gallé, Effect of drying on cement-based materials pore structure as identified by mercury intrusion porosimetry - a comparative study between oven-, vacuum-, and freeze-drying, Cement Concr. Res. 31 (2001) 1467–1477, https://doi.org/10.1016/S0008-8846(01)00594-4.

[53] V.M. Malhotra, Handbook of analytical techniques in concrete science and technology. http://www.sciencedirect.com/science/article/pii/B9780815514374500205, 2001.
[54] R.A. Cook, K.C. Hover, Mercury porosimetry of hardened cement pastes, Cement Concr. Res. 29 (1999) 933–943, https://doi.org/10.1016/S0008-8846(99)00083-6.
[55] E.W. Washburn, The dynamics of capillary flow, Phys. Rev. 17 (1921) 273–283, https://doi.org/10.1103/PhysRev.17.273.
[56] V. Cnudde, M.N. Boone, High-resolution X-ray computed tomography in geosciences: a review of the current technology and applications, Earth Sci. Rev. 123 (2013) 1–17, https://doi.org/10.1016/j.earscirev.2013.04.003.
[57] P.J. Withers, C. Bouman, S. Carmignato, V. Cnudde, D. Grimaldi, C.K. Hagen, E. Maire, M. Manley, A. Du Plessis, S.R. Stock, X-ray computed tomography, Nat. Rev. Methods Prim. 1 (2021) 1–21, https://doi.org/10.1038/s43586-021-00015-4.
[58] B. Masschaele, M. Dierick, D. Van Loo, M.N. Boone, L. Brabant, E. Pauwels, V. Cnudde, L. Van Hoorebeke, HECTOR: a 240kV micro-CT setup optimized for research, J. Phys. Conf. Ser. 463 (2013), https://doi.org/10.1088/1742-6596/463/1/012012.
[59] J. Vlassenbroeck, M. Dierick, B. Masschaele, V. Cnudde, L. Van Hoorebeke, P. Jacobs, Software tools for quantification of X-ray microtomography at the UGCT, Nucl. Instruments Methods Phys. Res. Sect. A Accel. Spectrometers, Detect. Assoc. Equip. 580 (2007) 442–445, https://doi.org/10.1016/j.nima.2007.05.073.
[60] L. Brabant, J. Vlassenbroeck, Y. De Witte, V. Cnudde, M.N. Boone, J. Dewanckele, L. Van Hoorebeke, Three-dimensional analysis of high-resolution X-ray computed tomography data with morpho+, Microsc. Microanal. 17 (2011) 252–263, https://doi.org/10.1017/S1431927610094389.
[61] F. Collins, J.G. Sanjayan, Effect of pore size distribution on drying shrinkage of alkali-activated slag concrete, Cement Concr. Res. 30 (2000) 1401–1406, https://doi.org/10.1016/S0008-8846(00)00327-6.
[62] P. Sikora, M. Techman, K. Federowicz, A.M. El-Khayatt, H.A. Saudi, M. Abd Elrahman, M. Hoffmann, D. Stephan, S.Y. Chung, Insight into the microstructural and durability characteristics of 3D printed concrete: cast versus printed specimens, Case Stud. Constr. Mater. 17 (2022), e01320, https://doi.org/10.1016/J.CSCM.2022.E01320.
[63] S. Yu, M. Xia, J. Sanjayan, L. Yang, J. Xiao, H. Du, Microstructural characterization of 3D printed concrete, J. Build. Eng. 44 (2021), 102948, https://doi.org/10.1016/J.JOBE.2021.102948.
[64] J.G. Sanjayan, B. Nematollahi, M. Xia, T. Marchment, Effect of surface moisture on inter-layer strength of 3D printed concrete, Construct. Build. Mater. 172 (2018) 468–475, https://doi.org/10.1016/j.conbuildmat.2018.03.232.
[65] N. Neithalath, J. Jain, Relating rapid chloride transport parameters of concretes to microstructural features extracted from electrical impedance, Cement Concr. Res. 40 (2010) 1041–1051, https://doi.org/10.1016/J.CEMCONRES.2010.02.016.
[66] V. Shah, J. Mackechnie, A. Scott, Determination of carbonation resistance of concrete through a combination of cement content and tortuosity, J. Build. Eng. 60 (2022), 105176, https://doi.org/10.1016/J.JOBE.2022.105176.
[67] P. Yang, G. Sant, N. Neithalath, A refined, self-consistent Poisson-Nernst-Planck (PNP) model for electrically induced transport of multiple ionic species through concrete, Cem. Concr. Compos. 82 (2017) 80–94, https://doi.org/10.1016/J.CEMCONCOMP.2017.05.015.
[68] R.W. Vervoort, S.R. Cattle, Linking hydraulic conductivity and tortuosity parameters to pore space geometry and pore-size distribution, J. Hydrol. 272 (2003) 36–49, https://doi.org/10.1016/S0022-1694(02)00253-6.
[69] C.E. Salmas, G.P. Androutsopoulos, A novel pore structure tortuosity concept based on nitrogen sorption hysteresis data, Ind. Eng. Chem. Res. 40 (2001) 721–730, https://doi.org/10.1021/ie000626y.
[70] G.P. Androutsopoulos, C.E. Salmas, A SIMPLIFIED MODEL FOR MERCURY POROSIMETRY HYSTERESIS, vol. 176, 2007, pp. 1–42, https://doi.org/10.1080/00986449908912144.
[71] G.P. Androutsopoulos, C.E. Salmas, Tomography of MACRO-MESO-PORE structure based on mercury porosimetry hysteresis loop scanning Part II, MP Hysteresis Loop Scanning Along the Overall Retraction Line 181 (2007) 179–202, https://doi.org/10.1080/00986440008912820.
[72] K. Li, Q. Zeng, M. Luo, X. Pang, Effect of self-desiccation on the pore structure of paste and mortar incorporating 70% GGBS, Construct. Build. Mater. 51 (2014) 329–337, https://doi.org/10.1016/J.CONBUILDMAT.2013.10.063.
[73] G. Bernardo, A. Telesca, G.L. Valenti, A porosimetric study of calcium sulfoaluminate cement pastes cured at early ages, Cement Concr. Res. 36 (2006) 1042–1047, https://doi.org/10.1016/j.cemconres.2006.02.014.
[74] I. Dressler, N. Freund, D. Lowke, The effect of accelerator dosage on fresh concrete properties and on interlayer strength in shotcrete 3D printing, Materials 13 (2020) 374, https://doi.org/10.3390/ma13020374.
[75] Y. Villagrán-zaccardi, N. Alderete, P. Van den Heede, N. De Belie, Pore size distribution and surface multifractal dimension by multicycle mercury intrusion porosimetry of ggbfs and limestone powder blended concrete, Appl. Sci. 11 (2021) 4851, https://doi.org/10.3390/app11114851.
[76] C. Sparrow, B. Mandelbrot, The Fractal Geometry of Nature, W.H. Freeman and company, 1984, https://doi.org/10.2307/2981858.
[77] B. Zhang, W. Liu, X. Liu, Scale-dependent nature of the surface fractal dimension for bi- and multi-disperse porous solids by mercury porosimetry, Appl. Surf. Sci. 253 (2006) 1349–1355, https://doi.org/10.1016/j.apsusc.2006.02.009.
[78] Q. Zeng, M. Luo, X. Pang, L. Li, K. Li, Surface fractal dimension: an indicator to characterize the microstructure of cement-based porous materials, Appl. Surf. Sci. 282 (2013) 302–307, https://doi.org/10.1016/j.apsusc.2013.05.123.
[79] Y. Gao, J. Jiang, G. De Schutter, G. Ye, W. Sun, Fractal and multifractal analysis on pore structure in cement paste, Construct. Build. Mater. 69 (2014) 253–261, https://doi.org/10.1016/j.conbuildmat.2014.07.065.
[80] H.M. Jennings, J.W. Bullard, J.J. Thomas, J.E. Andrade, J.J. Chen, G.W. Scherer, 113037917 5-29 Characterization and modeling of pores and surfaces in cement paste: correlations to processing and properties, J. Adv. Concr. Technol. 6 (2008) 5–29, https://doi.org/10.3151/jact.6.5.
[81] D. Gastaldi, G. Paul, L. Marchese, S. Irico, E. Boccaleri, S. Mutke, L. Buzzi, F. Canonico, Hydration products in sulfoaluminate cements: evaluation of amorphous phases by XRD/solid-state NMR, Cement Concr. Res. 90 (2016) 162–173, https://doi.org/10.1016/j.cemconres.2016.05.014.
[82] B. Xiao, Q. Huang, B. Yu, G. Long, H. Chen, A fractal model for predicting oxygen effective diffusivity of porous media with rough surfaces under dry and wet conditions, Fractals 29 (2021), https://doi.org/10.1142/S0218348X21500766.
[83] B. Yu, P. Cheng, A fractal permeability model for bi-dispersed porous media, Int. J. Heat Mass Tran. 45 (2002) 2983–2993, https://doi.org/10.1016/S0017-9310(02)00014-5.
[84] P. Yu, Y.H. Duan, E. Chen, S.W. Tang, X.R. Wang, Microstructure-based fractal models for heat and mass transport properties of cement paste, Int. J. Heat Mass Tran. 126 (2018) 432–447, https://doi.org/10.1016/j.ijheatmasstransfer.2018.05.150.
[85] N. Otsu, Threshold selection method from gray-level histograms, IEEE Trans Syst Man Cybern. SMC- 9 (1979) 62–66, https://doi.org/10.1109/tsmc.1979.4310076.
[86] A.A. Malcolm, H.Y. Leong, A.C. Spowage, A.P. Shacklock, Image segmentation and analysis for porosity measurement, J. Mater. Process. Technol. 192–193 (2007) 391–396, https://doi.org/10.1016/j.jmatprotec.2007.04.041.
[87] S. Divya Rani, A.V. Rahul, M. Santhanam, A multi-analytical approach for pore structure assessment in historic lime mortars, Construct. Build. Mater. 272 (2021), 121905, https://doi.org/10.1016/j.conbuildmat.2020.121905.
[88] V. Cnudde, A. Cwirzen, B. Masschaele, P.J.S. Jacobs, Porosity and microstructure characterization of building stones and concretes, Eng. Geol. 103 (2009) 76–83, https://doi.org/10.1016/j.enggeo.2008.06.014.
[89] V. Brunello, C. Canevali, C. Corti, T. De Kock, L. Rampazzi, S. Recchia, A. Sansonetti, C. Tedeschi, V. Cnudde, Understanding the microstructure of mortars for cultural heritage using X-ray CT and MIP, Materials 14 (2021) 5939, https://doi.org/10.3390/ma14205939.